ESTIMATES OF SPACECRAFT ATTITUDE AND SENSOR PARAMETERS USING ADAPTIVE FILTERING: METEOSAT-I TRANSFER ORBIT APPLICATION

G. Moek

National Aerospace Laboratory NLR
Amsterdam, The Netherlands

C.R. Traas

Twente University of Technology
Enschede, The Netherlands

ABSTRACT

In practical applications of Kalman filtering theory often inconsistencies between real estimation errors and computed errorvariances occur due to modelling errors. An adaptive filtering technique has been developed at NLR to deal with this filter divergence problem. Special attention is paid to divergence detection. When divergence is detected, adaptation is applied with an intensity governed directly by the intensity of the divergence detected.
This technique has been applied to METEOSAT-I transfer orbit flight data. Modelling errors are due to simple modelling of spacecraft dynamics and sensors. Spacecraft attitude and earth sensor delays have been estimated. Results, based on different combinations of sun aspect angle, earth chord and midscan rotation angle measurements show that in all these cases reliable estimates can be found.

Keywords: Adaptive filtering, Filter divergence, Modelling errors, Attitude, Sensors, Measurements.

1. INTRODUCTION

The Kalman filter approach to spacecraft attitude and parameter estimation is by now well established. It yields in least squares sense, the best linear estimate of the system state from noisy measurements. The estimate is computed recursively by processing a new measurement as it comes available. The main advantages of such a recursive approach are, generally, a reduction of the computational burden as compared with a batch processing method and the possibility to monitor the course of the estimation proces in real time. The Kalman filter explicitly yields a measure for the estimation errors in the form of the error covariance matrix.

Inputs for the Kalman approach are models of the system dynamics, the measurements and the noise statistics as well as a priori knowledge about the state. Errors in these inputs may lead to filter divergence. Roughly speaking this means that the error variances, computed as part of the filter, become unrealistically small in comparison with the real estimation errors. Therefore, what is needed in practice is not the plain Kalman filter, but a filter supplied with a mechanism that accounts for the effect of possible modelling errors. Various techniques, ranging from simple (periodic) restarts of the filter to very complicated estimation algorithms have been used in specific practical applications. Research in digital filtering techniques at the National Aerospace Laboratory NLR has led to an attractive generally applicable approach. It consists of an on line filter divergence detection and adaptation algorithm. The amount of adaptation is governed directly by the intensity of the divergence detected. To provide the filter with an accurate measurement noise statistic, a recursive measurement noise variance estimator is also available.

In this paper some results are presented of an application to in-flight measurements produced by the METEOSAT-I spacecraft in its transfer orbit. Very simple spacecraft- and sensormodels are used. The object is to show that for a well-observable system the adaptive filter can cope with the resulting modelling errors. Compared with previous work, observability is improved by using more flexible but still simple earth sensormodels. Estimation results based on different combinations of sun aspect angle, infra-red earth chord and midscan rotation angle measurements are compared.
The paper is built up as follows. In section 2 an outline of the modelling is given. In section 3 the measurements are described in detailed mathematical terms. Sections 4 and 5 contain a description of the filter and some filtering results. Section 6 contains conclusions.

2. OUTLINE OF SPACECRAFT AND ATTITUDE SENSOR MODELLING

For the purpose of filtering the ESA meteorological spacecraft METEOSAT-I is modelled here as a rigid spinner without nutation. External torques, possibly acting on the spacecraft are not modelled. With this model the spinaxis direction and the spin velocity are constants.

The spacecraft attitude is described by the orientation of the Body Reference Frame $\underline{X}_B$ with respect to the Celestial Reference Frame $\underline{X}_C$. Both frames are orthogonal coordinate systems. The Body Reference Frame $\underline{X}_B$ is a principal axis frame with the Z_B-axis chosen to coincide nominally with the spinvector and the $\underline{X}_B$-axis passing through some fixed point in the spacecraft equatorial plane. The Celestial Reference Frame $\underline{X}_C$ is an earth centered equatorial inertially oriented coordinate system, with the $\underline{X}_C$-axis in the direc-

Proc. Int. Symp. Spacecraft Flight Dynamics, Darmstadt, FRG, 18-22 May 1981 (ESA SP-160, Aug. 1981)

tion of the vernal equinox of 1950, Jan 1.0.

The mutual orientation between the body- and celestial reference frames is described by three angles ψ, θ and φ. Starting with the $\underline{X}_C$ system, turning an angle φ around the $\underline{X}_C$-axis yields an intermediate reference frame $\underline{X}_1$. Another intermediate reference frame $\underline{X}_2$ is found by turning an angle θ around the Y_1-axis. Finally, the Body Reference Frame $\underline{X}_B$ is arrived at by turning an angle ψ around the Z_2-axis. The rotation matrix T_{CB} defined by

$$\underline{X}_C = T_{CB}(\varphi,\theta,\psi)\,\underline{X}_B$$

is then given through

$$T_{CB} = \begin{pmatrix} C\theta C\psi & -C\theta S\psi & S\theta \\ S\varphi S\theta C\psi+C\varphi S\psi & -S\varphi S\theta S\psi+C\varphi C\psi & -S\varphi C\theta \\ -C\varphi S\theta C\psi+S\varphi S\psi & C\varphi S\theta S\psi+S\varphi C\psi & C\varphi C\theta \end{pmatrix}$$

where $C\theta = \cos(\theta)$, $S\varphi = \sin(\varphi)$ etc.

It follows from the spacecraft dynamic model that the spinaxis attitude is completely defined by the attitude angles φ and θ and that the phase angle ψ is not relevant for the present study.

The attitude measurement system of METEOSAT-I consists of two V-slit sun sensors and four pencil-beam infra-red earth sensors. Measurements of these sensors have been used in a preprocessed form. Thus, for the V-slit sun sensors, slit passage times preprocessed to angular velocity and to solar aspect angle (Fig. 1) have been used. A pencil-beam earth sensor measures times of earth horizon passage. Of each earth sensor the times of space/earth and earth/space passage, converted to earth chord and sun-earth midscan rotation angle (Figs. 2 and 3) have been used. In table 1 the mounting angles with respect to the spacecraft equator plane are given for the four infra-red sensors.

For each of the infra-red earth sensors it is assumed that both S/E and E/S passage times are affected by unknown delays. The magnitude of the delays depends in a complicated way on the geometrical configuration of sensor and earth. When an adaptive filtering technique is used, this relationship can be modelled rather simply because the purpose of the adaptation is to mask the resulting modelling errors. It was assumed in reference 2, therefore, that except in case of short chord lengths, the resulting delay of an earth chord measurement could be approximated by a constant. However, it was found that such modelling was not flexible enough to yield completely satisfactory results. It was also found from plots of earth chord measurement residuals based on an ESOC attitude estimate that the delays varied approximately linearly in time (See figures 7 and 8). In the present paper, therefore, the delay of any earth horizon passage time is modelled as a linear function of time. The earth itself is considered to be a sphere with radius R_E = 6420.0 km (Ref.5).

3. MEASUREMENT RELATIONS

The measurements depend non-linearly on the attitude angles φ and θ. Thus, linearized measurement equations are derived to be used by the (extended) Kalman filter of section 4.

3.1 The measurement data file

METEOSAT-I transfer orbit flight data were obtained from an ESOC archive file. Specifically, this file contained the following data: spacecraft position in $\underline{X}_C$ coordinates, unit vector from spacecraft towards sun in $\underline{X}_C$ coordinates, solar aspect angle, sun-S/E and sun-E/S rotation angle and earth chord per active infra-red earth sensor.

3.2 Sun sensor measurements

The sun sensor measurements are solar aspect angle measurements (Fig. 1). The solar aspect angle χ_S is related geometrically to the attitude angles φ and θ through

$$\cos\chi_S = i_{S_1}\sin\theta - i_{S_2}\sin\varphi\cos\theta + i_{S_3}\cos\varphi\cos\theta \qquad (1)$$

where i_{S_1}, i_{S_2} and i_{S_3} are the components of the unit vector from the spacecraft to the sun expressed in $\underline{X}_C$, $(\underline{i}_{sun})_C = (i_{S_1}, i_{S_2}, i_{S_3})^T$.

Linearization of equation (1) yields the measurement equation (2) which is to be used in the filter:

$$\delta\chi_S = \left(\frac{A}{C}\ \ \frac{B}{C}\right)\begin{pmatrix}\delta\varphi\\ \delta\theta\end{pmatrix} \qquad (2)$$

with

$$A = i_{S_2}\cos\varphi\cos\theta + i_{S_3}\sin\varphi\cos\theta$$

$$B = -i_{S_1}\cos\theta - i_{S_2}\sin\varphi\sin\theta + i_{S_3}\cos\varphi\sin\theta \qquad (3)$$

$$C = \sin\chi_S$$

3.3 Earth sensor measurements

3.3.1 Infra-red earth chord measurements

Figure 2 shows one half of the trajectory traced by an infra-red sensor over the earth. The following geometrical relation exists between the earth chord γ_g, the earth aspect angle χ_E, the angular semi-diameter of the earth α and the offset angle of sensor with respect to spacecraft equatorial plane δ:

$$\cos\alpha = \cos\chi_E\sin\delta + \sin\chi_E\cos\delta\cos\tfrac{1}{2}\gamma_g \qquad (4)$$

The earth aspect angle χ_E is related to the attitude angles φ and θ through

$$\cos\chi_E = \frac{1}{r_s}\left(-X_s\sin\theta + Y_s\sin\varphi\cos\theta - Z_s\cos\varphi\cos\theta\right) \qquad (5)$$

where, X_s, Y_s, Z_s are the position coordinates of the spacecraft in the $\underline{X}_C$ frame and r_s is the distance between spacecraft and centre of the earth. Equations (4) and (5) describe the relation between the earth chord γ_g and the angles φ and θ. The angle α is found from

$$\sin\alpha = R_E/r_s \qquad (6)$$

where R_E is the earth radius.

Linearization of the equations (4) and (5) gives

$$\delta\gamma_g = (C_E A_E \quad C_E B_E)\begin{pmatrix}\delta\varphi\\ \delta\theta\end{pmatrix} \tag{7}$$

where

$$A_E = -\frac{(Y_s \cos\varphi + Z_s \sin\varphi)\cos\theta}{r_s \sin\chi_E}$$

$$B_E = \frac{X_s \cos\theta + (Y_s \sin\varphi - Z_s \cos\varphi)\sin\theta}{r_s \sin\chi_E} \tag{8}$$

$$C_E = \frac{2\cos\chi_E \cos\delta \cos\tfrac{1}{2}\gamma_g - \sin\chi_E \sin\delta}{\sin\chi_E \cos\delta \sin\tfrac{1}{2}\gamma_g}$$

The actually measured chord length γ differs from the geometric chord length γ_g due to a delay of an infra-red sensor. Denoting delays of the S/E and E/S passages by d_1 and d_2 (radians) respectively, it follows that

$$\gamma = \gamma_g + (d_2 - d_1) \tag{9}$$

For each infra-red sensor the delays d_1 and d_2 are modelled as linear functions of time, i.e.

$$d_1 = a_1 + b_1 \Delta t \quad , \quad d_2 = a_2 + b_2 \Delta t \tag{10}$$

where a_1, b_1, a_2 and b_2 are constants and Δt denotes the time difference $\Delta t = t - t_{reference}$. When solar aspect angle and earth chord measurements are used in the filter, the difference $c = a + b\Delta t$ of the delays d_2 and d_1 may be estimated per sensor. The delays can be estimated individually when also the midscan rotation angle measurements (see below) are used. Taking the delays into account, the measurement equation (7) for a particular infra-red sensor becomes for both cases

$$\delta\gamma_g = (C_E A_E \quad C_E B_E \quad 1 \quad \Delta t)\begin{pmatrix}\delta\varphi\\ \delta\theta\\ \delta a\\ \delta b\end{pmatrix} \tag{11}$$

and

$$\delta\gamma_g = (C_E A_E \quad C_E B_E \quad -1 \quad -\Delta t \quad 1 \quad \Delta t)\begin{pmatrix}\delta\varphi\\ \delta\theta\\ \delta a_1\\ \delta b_1\\ \delta a_2\\ \delta b_2\end{pmatrix} \tag{12}$$

3.3.2 Sun-earth midscan rotation angle measurements

In figure 3 the sun-earth midscan rotation angle ρ_g is defined. From spherical geometry it follows that

$$\cos\chi = \cos\chi_S \cos\chi_E + \sin\chi_S \sin\chi_E \cos\rho_g \tag{13}$$

where

$$\cos\chi = -\frac{1}{r_s}(i_{S_1} X_s + i_{S_2} Y_s + i_{S_3} Z_s) \tag{14}$$

and the solar- and earth aspect angles χ_S and χ_E are defined by equations (1) and (5). Thus, equations (1), (5), (13) and (14) describe the relation between the midscan rotation angle ρ_g and the attitude angles φ and θ.

Linearization of equation (13) yields

$$\delta\rho_g = (A_M \frac{A}{C} + B_M A_E \quad A_M \frac{B}{C} + B_M B_E)\begin{pmatrix}\delta\varphi\\ \delta\theta\end{pmatrix} \tag{15}$$

where

$$A_M = \frac{-\sin\chi_S \cos\chi_E + \cos\rho_g \cos\chi_S \sin\chi_E}{\sin\chi_S \sin\chi_E \sin\rho_g}$$

$$B_M = \frac{-\cos\chi_S \sin\chi_E + \cos\rho_g \sin\chi_S \cos\chi_E}{\sin\chi_S \sin\chi_E \sin\rho_g} \tag{16}$$

and A, B, A_E and B_E are defined by (3) and (8).

As for the earth chord measurement, the measured midscan rotation angle ρ consists of a geometrical part and a delay. Because the preprocessed measurement is the average of two rotation angles, it follows that

$$\rho = \rho_g + (d_1 + d_2)/2$$

where d_1 and d_2 refer to the delay of the S/E and E/S passages respectively. When solar aspect angle- and midscan rotation angle measurements are used in the filter, the average delay $\bar{c} = \bar{a} + \bar{b}\Delta t$ per sensor can be estimated. Using also the earth chord measurements the delays d_1 and d_2 can be estimated individually. The measurement equation for a specific earth sensor becomes for these two cases

$$\delta\rho_g = (A_M \frac{A}{C} + B_M A_E \quad A_M \frac{B}{C} + B_M B_E \quad 1 \quad \Delta t)\begin{pmatrix}\delta\varphi\\ \delta\theta\\ \delta\bar{a}\\ \delta\bar{b}\end{pmatrix} \tag{17}$$

and

$$\delta\rho_g = (A_M \frac{A}{C} + B_M A_E \quad A_M \frac{B}{C} + B_M B_E \quad \tfrac{1}{2} \quad \tfrac{1}{2}\Delta t \quad \tfrac{1}{2} \quad \tfrac{1}{2}\Delta t)\begin{pmatrix}\delta\varphi\\ \delta\theta\\ \delta a_1\\ \delta b_1\\ \delta a_2\\ \delta b_2\end{pmatrix} \tag{18}$$

4. THE ADAPTIVE FILTER

In this section the adaptive Kalman filter and a recursive measurement noise variance estimator are described. The emphasis in the description is on the features that are different from the plain Kalman filter.

4.1 Basic time- and measurement update

In the previous section different combinations of measurements have already been mentioned. The combinations actually considered in this paper are

1. sun aspect angle and earth chord
2. sun aspect angle and earth chord and midscan rotation angle.

In both cases the attitude angles φ and θ are estimated. The remaining parameters depend on the combination of measurements used. For combination 1. the earth chord delay parameters a_i and b_i, $i = 1,\ldots,4$ defining the delay $c_i = a_i + b_i\Delta t$ are estimated. For combination 2. the earth horizon passage delay parameters a_{ij} and b_{ij}, $i = 1,\ldots,4$, $j = 1,2$ defining the S/E and E/S passage delays $d_{ij} = a_{ij} + b_{ij}\Delta t$ are estimated. Thus, the dimension of the state vector X is 10 or 18:

$$X = (\varphi\ \theta\ a_1\ b_1\ a_2\ b_2\ a_3\ b_3\ a_4\ b_4)^T$$

or

$$X = (\varphi\ \theta\ a_{11}\ b_{11}\ a_{12}\ b_{12}\ a_{21}\ b_{21}\ a_{22}\ b_{22}\ a_{31}\ b_{31}\ a_{41}\ b_{41}\ a_{42}\ b_{42})^T$$

Because the state vector elements are modelled as constants, the time update of the filter is trivial in the absence of adaptation. The measurement update itself does not differ from the usual one in the extended Kalman filter. Therefore, a detailed description of the basic time update and the measurement update can be omitted here. It suffices to remark that the actual filter computations are done in square root form because this gives better numerical performance.

4.2 Divergence, detection and adaptation

The simple modelling proposed in section 2 can lead to filter divergence when no special measures such as adaptation are taken. The filter divergence problem may be sketched as follows. Between measurement updates, state estimates are propagated through the system dynamics model. Any errors in this model as well as in the "input" estimates will lead to errors in the propagated estimates. The measurements, containing information about the actual state are to correct such errors (in a least squares sense). However, the weight on the new measurements in the measurement update is determined by the ratio of the uncertainty in the measurements themselves (measurement noise variance) to the uncertainty in the predicted estimates at the time of the measurement as characterized by the predicted error covariance matrix. As the filter is unaware of modelling errors, the error covariance matrix decreases monotonically (at least in the absence of system noise) as more and more measurements are processed. This results in the measurements getting too low a weight in the measurement update, i.e. the measurements lose their corrective power. The estimation process then gets governed largely by the system dynamics. Thus, in case of modelling errors the consistency between the actual estimation errors and the computed error variances tends to get lost. As modelling errors are virtually always present (whether intentional or unknown), a mechanism is needed to monitor filter performance. In fact, any such a mechanism must be based on the available measurement residuals.

The following algorithm is used to detect improper filter performance or filter divergence. Let z and $\tilde{z}$ be the actual and predicted measurement at the same time t. The difference $r=z-\tilde{z}$ is called the measurement residual at time t. Writing

$$r = M(X_{exact} - \tilde{X}) + w$$

where w represents measurement noise, it follows immediately that

$$E\{r\} = 0, \qquad E\{r^2\} = M\tilde{\Lambda}M^T + \sigma_w^2$$

where $\tilde{\Lambda}$ is the predicted error covariance matrix and σ_w^2 the measurement noise variance. When the filter does not operate properly for some reason, the above statistics will generally not be satisfied. Therefore, two succeeding tests, based on the measurement residuals are performed before the measurement update.
The first test is whether

$$\tfrac{1}{2}(r_k^2 + r_{k+1}^2) > 3\,(M_{k+1}\tilde{\Lambda}_{k+1}M_{k+1}^T + \sigma_{w_{k+1}}^2) \qquad (19)$$

If this holds, then a switching parameter c is given the value 1, otherwise the value 0. This stepwise variable parameter c is used as input into a second order low pass filter:

$$\frac{d^2y}{d\tau^2} + 2p\frac{dy}{d\tau} + p^2 y = cp^2 \qquad (20)$$

$$y(0) = dy/d\tau(0) = 0$$

The variable τ is a normalised time variable such that $\tau_{k+1} - \tau_k = 1$ for all k, whereas the parameter p is a filter constant. Discretizing eq. (20), the output sequence y_k is found. For $p = .223$ the time constant of the filter (20) is 4.5 measurements which experimentally has been found to be suitable (Ref. 2). For $c_k \equiv 0$, the solution of equation (20) tends to zero, whereas for $c_k \equiv 1$ it tends to 1. Experimentally again, it has been found that a second test on the output sequence y_k achieves much better discrimination between divergence and non-divergence than the test (19) on the measurement residuals directly.
The second test is whether

$$y_{k+1} > 0.15 \qquad (21)$$

If this test is satisfied, the filter is said to diverge and an on-line adaptive action is performed to restore proper filter performance. When the second test is not satisfied, no special action is taken.

When the filter is found to diverge, it is concluded that modelling errors are present. These are accounted for by introducing noise into the system dynamic model. Thus, uncertainty is added to the predicted state estimate which indirectly increases the weight on the measurements in the measurement update. In many cases a direct physical interpretation of the additional system noise is possible. For the present application this approach yields

$$\dot{X} = \Gamma\xi$$

where ξ is a noise vector with statistics

$$E\{\xi\} = 0, \qquad E\{\xi\xi^T\} = \Lambda_\xi$$

and where the matrix Γ distributes the elements of ξ suitably over the elements of $\dot{X}$. The values of the elements of Λ_ξ are controlled by the divergence monitoring parameter y_k. The time up-

date which preceeds the measurement update is no longer trivial for a diverging filter. The prediction of the state vector itself remains unchanged, but the covariance matrix prediction is modified. Although the actual computations are done in square root form, the result is described here directly for the predicted covariance matrix. Assuming that Γ is a constant matrix and that ξ is a stepwise constant random variable between any two successive measurements, it is found that

$$\tilde{\Lambda}_{k+1} = \hat{\Lambda}_k + G_{k+1}\,\Lambda_{\xi_k}\,G_{k+1}^T$$

where $G_{k+1} \overset{\Delta}{=} (t_{k+1} - t_k)\Gamma.\hat{\Lambda}_k$ is the basic predicted error covariance matrix at time t_{k+1} before divergence detection and adaptation. $\tilde{\Lambda}_{k+1}$ is the predicted error covariance matrix after the divergence detection tests. It is equal to $\hat{\Lambda}_k$ when no divergence is detected and equal to the above expression when divergence has been detected indeed. For Λ_ξ a diagonal matrix is chosen. Its form is dependent on the measurement being processed, because only those elements of $\hat{\Lambda}_k$ are adapted that correspond with the state vector elements involved in the measurement. Thus, for solar measurements

$$\Lambda_\xi^{2x2} = \begin{pmatrix} \sigma^2_{\xi_\varphi} & 0 \\ 0 & \sigma^2_{\xi_\theta} \end{pmatrix}, \qquad G^{18x2} = \begin{pmatrix} \Delta t & 0 \\ 0 & \Delta t \\ \multicolumn{2}{c}{\bigcirc} \end{pmatrix}$$

For infra-red earth measurements (regardless of the type) of sensor i (i=1, ..., 4):

$$\Lambda_\xi^{6x6} = \begin{pmatrix} \sigma^2_{\xi_\varphi} & & & & & \\ & \sigma^2_{\xi_\theta} & & & & \\ & & \sigma^2_{\xi_{a_{i1}}} & & & \\ & & & \sigma^2_{\xi_{b_{i1}}} & & \\ & & & & \sigma^2_{\xi_{a_{i2}}} & \\ & & & & & \sigma^2_{\xi_{b_{i2}}} \end{pmatrix}$$

$$G^{18x6} = \begin{pmatrix} \Delta t & 0 & & & & \\ 0 & \Delta t & & & & \\ \multicolumn{6}{c}{\bigcirc} \\ & & \Delta t & 0 & 0 & 0 \\ & & 0 & \Delta t & 0 & 0 \\ & & 0 & 0 & \Delta t & 0 \\ & & 0 & 0 & 0 & \Delta t \end{pmatrix} \leftarrow \text{row } 2+(i-1)*4+1$$

Notice that here all matrices are defined for the case of an 18-dimensional statevector, thus when all three types of measurements are used.

For each type of measurement and each sensor a separate monitoring parameter y is used and the value of any σ^2_ξ is determined by the y-parameter corresponding with the measurement under consideration. Let $\hat{\sigma}^2_k$ be any (trivially) predicted variance which is to be adapted and let y_{k+1} denote the divergence monitoring parameter involved. Then the following algorithm is applied:

$$\sigma^2_\xi = \frac{2}{(\Delta t)^2}\,\hat{\sigma}^2_k\,(y_{k+1}-0.15) \quad \text{if } y_{k+1} > 0.15$$

$$\sigma^2_\xi = 0 \quad \text{if } y_{k+1} \leq 0.15$$

Thus, in case of divergence (numerically defined by $y_{k+1} > 0.15$) the adapted predicted variances become

$$\tilde{\sigma}^2_{k+1} = \hat{\sigma}^2_{k+1}\,\{1 + 2\,(y_{k+1} - 0.15)\}$$

It follows that $\hat{\sigma}^2_k$ is multiplied by a factor ranging from 1.0 to 2.7, depending on the amount of divergence as determined by $y_{k+1}-0.15$.

4.3 Measurement noise estimation

The measurement noise variance of the infra-red earth measurements is estimated on line using the following set of equations (per sensor and per type of measurement):

$$\Delta t_{k+1} = \Delta t_k + 0.05\,\{|t_{k+1}-t_k| - \Delta t_k\}$$

$$\eta_{k+1} = z_{k+1} - z_k$$

$$\xi_{k+1} = \frac{\eta_{k+1}}{t_{k+1}-t_k}$$

$$\bar{\xi}_{k+1} = \bar{\xi}_k + 0.05\,\frac{|t_{k+1}-t_k|}{t_{k+1}}\,\{\xi_{k+1} - \bar{\xi}_k\}$$

$$(S^2_\eta)_{k+1} = (S^2_\eta)_k + 0.04[\{\eta_{k+1}-(t_{k+1}-t_k)\bar{\xi}_{k+1}\}^2 - (S^2_\eta)_k]$$

$$(\sigma^2_z)_{k+1} = \tfrac{1}{2}(S^2_\eta)_{k+1}$$

The meaning of the symbols in these expressions is

- t_k : time at which k-th measurement is available
- z_k : k-th measurement
- η : local measurement increment
- ξ : local rough slope) of measurements as
- $\bar{\xi}$: local mean slope) function of time
- S^2_η : sample variance of η
- σ^2_z : variance of z

The above algorithm is based on the assumptions that the measurement -time function z(t) is a linear function and that the variance of the measurement increment is constant. Under these conditions the estimates $(\sigma^2_z)_{k+1}$ can be shown to converge to the actual measurement noise variance. However, the algorithm has been found useful also under moderate deviations of these assumptions and is therefore used in the present paper.

For sun sensor measurements the following approach is used. A number of n sun measurements z_i is averaged and processed as a single measurement $\bar{z}$:

$$\bar{z} = \frac{1}{n} \sum_{i=1}^{n} z_i$$

The value of n (≤ 17) is determined from the structure of the datafile. The variance of the averaged measurement is estimated by

$$S_{\bar{z}}^2 = \frac{1}{n} \frac{\sum_{i=1}^{n} z_i^2 - \frac{1}{n}\left(\sum_{i=1}^{n} z_i\right)^2}{n-1} \left(1 + \sqrt{2/(n-1)}\right)$$

where the factor $1 + \sqrt{2/(n-1)}$ is used as a correction factor to account for the fact that the random sample on which the estimated variance is based is finite.

5. FILTERING RESULTS

In this section results of the adaptive filter applied to METEOSAT-I transfer orbit data are presented. In figure 4 the projection of the transfer orbit onto the X_c-Y_c coordinate plane is given. During 16 hours the transfer orbit has been passed through about one and a half times by the spacecraft. In the figure the various manoeuvres and free-drift periods are shown. Table 2 contains the spin axis attitude as estimated by ESOC for the various free-drift periods. Results are given for free-drift periods 4 and 2. To see what may be expected of the adaptive filter under fully controlled conditions a simulation of free-drift period 4 is discussed first.

5.1 Simulation of free-drift period 4

For this simulation, earth chord and solar aspect angle measurements have been generated. They are shown in figures 5 and 6. The following truth model data apply to this case:

- spin axis right ascension
  RA = 353.176°
- spin axis declination
  DECL = -22.646°
- sun sensor noise
  σ_w(sun) = 0.00024 rad
- earth sensor noise
  σ_w(earth chord) = 0.0011 rad

The geometrical configuration is such that near-collinearity (175°) occurs at t = 5000 sec and coplanarity around t = 4500 sec.

The simulated earth chord delays are shown in figure 17, whereas their numerical values are (time t in days, measured from the start of the simulation):

- delay of first earth chord, c_1=0.040-0.230 t
- delay of second earth chord, c_2=0.029+0.276 t
- delay of third earth chord, c_3=0.016-0.300 t

They are based on plots of earth chord measurement residuals computed for real free-drift period 4 using the ESOC spin axis attitude estimate: RA = 353.2° and DECL = -22.6°. See figures 7 and 8.

The filter was initialized with the following values:

$\tilde{a}_i$ = 0.0 $\quad \tilde{\sigma}_{a_i}$ = 0.02 rad (i=1,...,4)

$\tilde{b}_i$ = 0.0 $\quad \tilde{\sigma}_{b_i}$ = 0.10 rad/day (i=1,...,4)

$\tilde{RA}$ = 353.20° $\quad \tilde{\sigma}_{RA}$ = 1.15°

$\tilde{DECL}$ = -22.60° $\quad \tilde{\sigma}_{DECL}$ = 1.15°

Results are presented in figures 9 through 19. Almost throughout, the actual estimation errors are less than two computed standard deviations. During the initial period the maximum error is less than three computed standard deviations, but the a priori error in the slope of the delay-time function is also of this magnitude. Filter divergence is virtually absent due to the fact that no modelling errors were introduced. Therefore, state variance adaptation is activated rarely as can be seen from the plots of the standard deviations.
During the time that only the first earth sensor is active, the spin axis attitude estimates are almost fixed. As the attitude is already fairly well known there, the information from the measurements is mainly used to update the delay parameters.
This simulation shows that it is possible to estimate in addition to the spacecraft attitude both parameters in the earth chord delay models of the sensors involved. Near collinearity and coplanarity do not introduce any particular observability problems in this example.

5.2 Real free-drift period 4

The measurements available for real free-drift period 4 are plotted in figures 20, 21, and 22. The following combinations of measurements are used in the filter. The number of each type used is indicated between parentheses:

case 1. solar aspect angle (225)
+ earth chord (1030)
case 2. solar aspect angle (225) + earth chord (870) + midscan rotation angle (870)

Based on a post-AMF orbit matching procedure ESOC provides the following attitude estimates:

RA = 353.2°, $\quad$ DECL = -22.6°

with an accuracy of 0.1 degree.

Case 1
The filter was initialized with the same values as used in the simulation of free-drift period 4. The results are presented in figures 23 through 30. Figures 23 and 24 suggest that an average value for the constant spin axis attitude is

$\overline{RA}$ = 353.1°, $\quad \overline{DECL}$ = -22.6°

with an accuracy

$\bar{\sigma}_{RA}$ = 0.05°, $\quad \bar{\sigma}_{DECL}$ = 0.10°.

The difference between the estimated instantaneous spin axis attitude and the ESOC estimates is consistently less than four computed standard deviations. For the spin axis declination this difference is even less than 2 standard deviations from about t = 5000 sec onwards.

Near collinearity and coplanarity around t = 5000 and 3500 sec respectively do not seem to cause special problems. However, a considerable peak in the estimation errors occurs when the third earth sensor loses earth coverage and at the same time the first earth sensor starts operating. Due to the adaptation mechanism the computed standard deviations are increased accordingly.
The estimated earth chord delays are shown in fig.27. The on-line estimated earth chord measurement noise standard deviations were found to converge to approximately 0.0005 and 0.0006 rad for the third and first earth sensor respectively.

Case 2
Results for free-drift period 4 when also the midscan rotation angle is used in the filter are shown in figures 31 through 39. The filter was initialized with the same values as before, except for the delay parameters. There were initialized as

$$\left.\begin{array}{l} \tilde{a}_{ij}=0.0 \quad \tilde{\sigma}_{a_{ij}} = 0.02 \text{ rad} \\ \tilde{b}_{ij}=0.0 \quad \tilde{\sigma}_{b_{ij}} = 0.02 \text{ rad/day} \end{array}\right\} \begin{array}{l} i=1,\ldots,4 \\ j=1,2 \end{array}$$

Recall that with the additional measurement for each earth sensor four delay parameters are estimated.

The estimation errors as compared with the ESOC attitude are less than 3 to 4 computed standard deviations. The magnitude of the divergence monitoring parameters of the sun and earth chord measurements is similar to that for case 1. In addition, the monitoring parameter of the midscan rotation angle measurements of the first earth sensor indicates rather strong divergence around the change over from the third to the first earth sensor. As a consequence, the estimation process changes rather drastically as compared with the previous case. The cause of the modelling errors at this point is not yet clear.

The measurement noise standard deviation of the midscan rotation angle measurements as computed in open loop with the algorithm described in section 4.3 is approximately 0.0003 rad for the third and first earth sensor.
The computed standard deviation of the estimated earth chord delays is of the order 0.0006 and 0.0008 rad for both sensors. For the estimated delay of the midscan rotation angle measurements these numbers are 0.0003 and 0.0005 respectively.

5.3 Real free-drift period 2
During free-drift period 2 only the third earth sensor and the sun sensor were active. The following combinations and numbers (between parentheses) of measurements were used in the filter:

case 1. solar aspect angle (80) + earth chord (310)
case 2. solar aspect angle (80) + earth chord (280) + midscan rotation angle (280)

ESOC provides the following attitude estimates

$$RA = 4.0^{\circ}, \qquad DECL = -25.9^{\circ}$$

with an accuracy of 1.0° degree.
Near-collinearity occurs around t = 2500 sec.

Case 1
The filter was initialized with the following data

$$\begin{array}{llll} \tilde{a}_i = 0.0 & \tilde{\sigma}_{a_i} = 0.02 \text{ rad} & i=1,\ldots,4 \\ \tilde{b}_i = 0.0 & \tilde{\sigma}_{b_i} = 0.10 \text{ rad/day} & i=1,\ldots,4 \\ \tilde{RA} = 4.0 & \tilde{\sigma}_{RA} = 1.15^{\circ} & \\ \tilde{DECL} = -25.9 & \tilde{\sigma}_{DECL} = 1.15^{\circ} & \end{array}$$

Results are shown in figures 40 through 44. Figures 40 and 42 suggest as an average spin axis attitude estimate for free-drift period 2

$$\overline{RA} = 4.95^{\circ}, \qquad \overline{DECL} = -25.25$$

with an accuracy

$$\bar{\sigma}_{RA} = 0.10^{\circ}, \qquad \bar{\sigma}_{DECL} = 0.15^{\circ}$$

The difference between the peak values of the right ascension and declination is about 0.25 and 0.35 degree.
As can be seen from the plots of the standard deviations the adaptation mechanism is activated for a period of time around t = 4000 sec.

Case 2
Results for real free-drift period 2 based on the use of all three types of measurements in the filter are shown in figures 45 through 50. The filter was initialized with the same attitude data as for case 1. For the delay parameters the following data were used

$$\left.\begin{array}{l} \tilde{a}_{ij} = 0.0 \quad \tilde{\sigma}_{a_{ij}} = 0.02 \text{ rad} \\ \tilde{b}_{ij} = 0.0 \quad \tilde{\sigma}_{b_{ij}} = 0.02 \text{ rad} \end{array}\right\} \begin{array}{l} i=1,\ldots,4 \\ j=1,2 \end{array}$$

As an average estimate may be taken here

$$\overline{RA} = 4.97^{\circ}, \qquad \overline{DECL} = -25.25^{\circ}$$

with an accuracy of

$$\bar{\sigma}_{RA} = 0.10^{\circ}, \qquad \bar{\sigma}_{DECL} = 0.12^{\circ}$$

These attitude estimates as well as the estimated earth chord delay of figure 49 are in good agreement with the results of case 1.

6. CONCLUSIONS

Application of an adaptive recursive filtering technique to METEOSAT-I transfer orbit flight data has been described. Results were obtained for free-drift periods 2 and 4.
Delays of infra-red earth sensors have been modelled as linear functions of time and were estimated in addition to the spacecraft attitude.
Different combinations of sun aspect angle, earth chord and midscan rotation angle measurements have been used. For the first part of free-drift period 4, during which successively coplanarity and near-collinearity occurred, slightly better results have been obtained using all three types of measurements in the filter.

Comparison of the estimated spin axis attitude with a reference attitude for free-drift period 4 based on a post-AMF analysis shows that the maximum estimation errors are bounded by 3 to 4 computed standard deviations.
Thus, it is concluded that the adaptive filter can cope with the modelling errors caused by the use of relatively simple models. With that, its usefulness in practical filtering problems is shown.

7. REFERENCES

1. Jazwinski, A.H. Stochastic processes and filtering theory. Academic Press, 1970.

2. Traas, C.R., Moek, G. Processing of METEOSAT attitude measurement flight data and evaluation of the performance of an adaptive filtering technique. National Aerospace Laboratory NLR, The Netherlands, NLR TR 78146 U. ESA CR(P)-1218.

3. Gelb, A. (ed). Applied optimal estimation. M.I.T. Press 1974.

4. Wertz, J.R. (ed). Spacecraft attitude determination and control. Reidel Publishing Company, 1978.

5. Lagowski, R.G., Ferguson, R.J. Improved determination of Apogee Motor Pointing. Journal of spacecraft, vol. 13, no 1, 1976.

8. ACKNOWLEDGEMENT

This paper is based on work performed for the European Space Agency ESA under ESTEC contract no 3319/77 monitored by D. Sciacovelli, ESTEC, Noordwijk, The Netherlands and provided with flight data and technical comments by L. Fraiture, ESOC, Darmstadt, Germany.

TABLE 1

declination of IR sensors with respect to geometric spacecraft equator

IR sensor	declination
1	+ 3.73°
2	- 3.89°
3	+ 22.60°
4	- 49.88°

TABLE 2

Manoeuvres and free-drift periods.
Spin axis right ascension (RA) and declination (DECL) during free-drift periods.

Phase	RA	DECL	Accuracy
Nutation damping			
Free-drift 1	174.8°	-23.2 °	1.0 °
Course manoeuvre			
Free-drift 2	4.0°	-25.9 °	1.0 °
Fine manoeuvre			
Free-drift 3	352.4°	-22.2 °	0.15°
Hyperfine manoeuvre			
Free-drift 4	353.2°	-22.6 °	0.1 °
Apogee motor firing			
Free-drift 5	353.2°	-22.6 °	0.1 °
Spin axis erection			
Free-drift 6	115.9°	88.86°	0.3 °

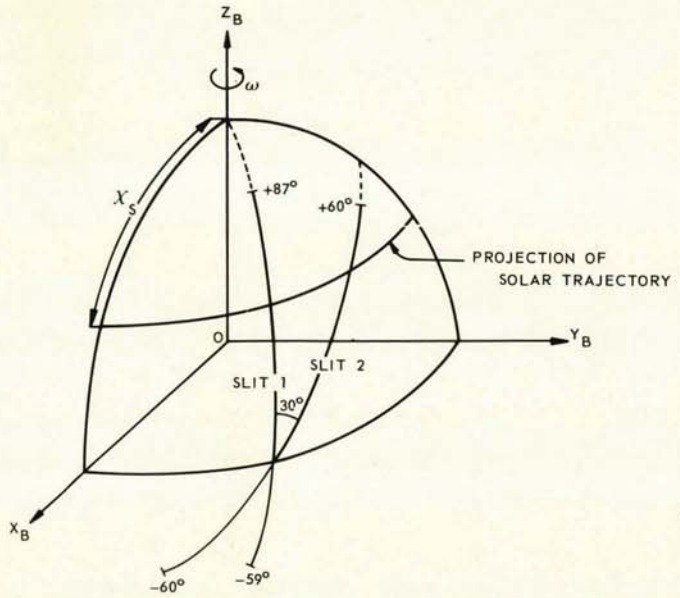

Fig. 1 The solar aspect angle sensor

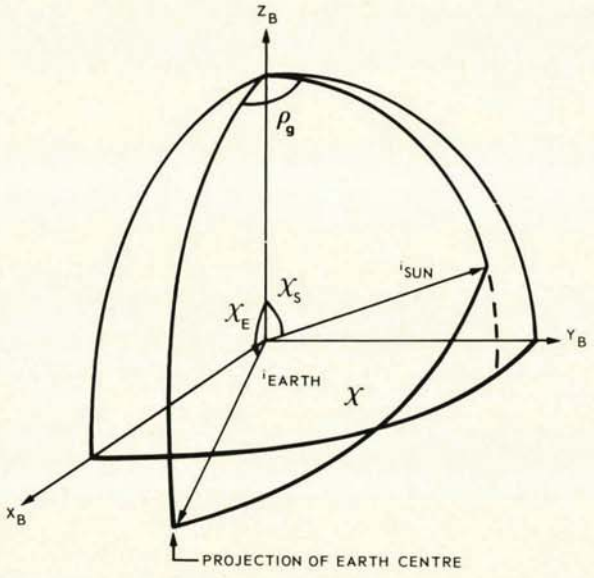

Fig. 3 Sun-earth midscan rotation angle ρ_g

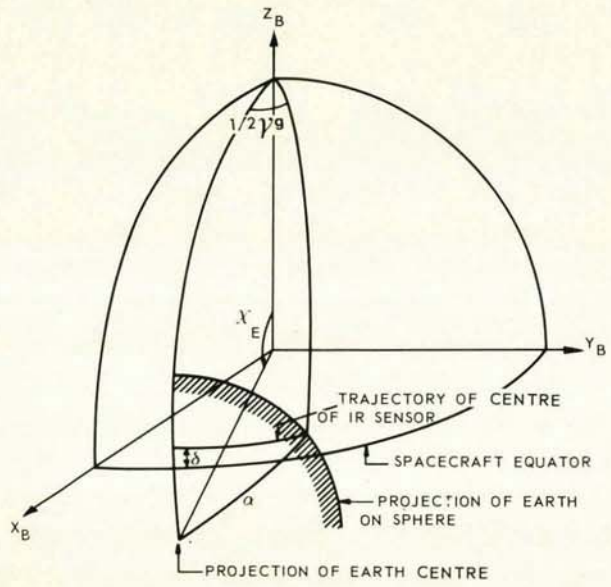

Fig. 2 Coverage of the earth by IR sensor

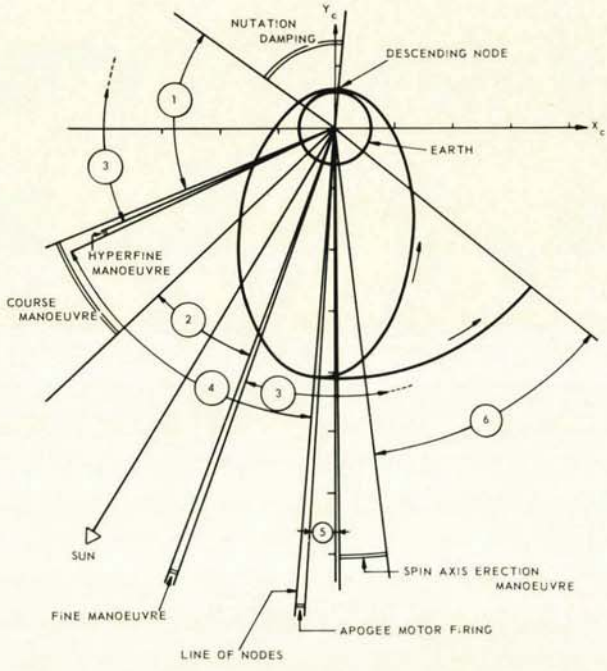

Fig. 4 Projection of orbit onto X_C, Y_C-plane, manoeuvre sequence and free-drift arcs

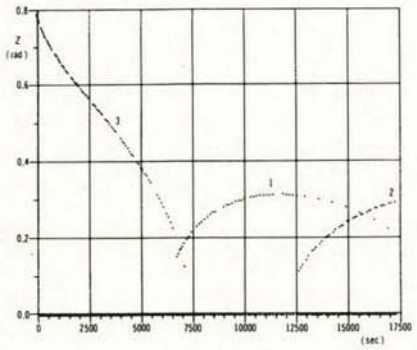

Fig. 5 Simulated earth chord measurements (simulation free-drift 4)

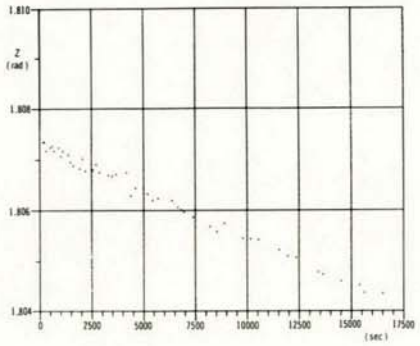

Fig. 6 Simulated sun measurements (simulation free-drift 4)

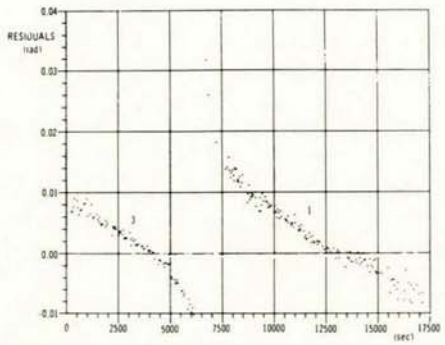

Fig. 7 Earth chord measurement residuals of first and third earth sensor, based upon ESOC attitude estimate (real free-drift 4)

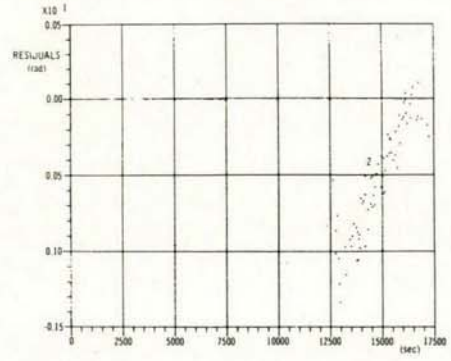

Fig. 8 Earth chord measurement residuals of second earth sensor, based upon ESOC attitude estimate (real free-drift 4)

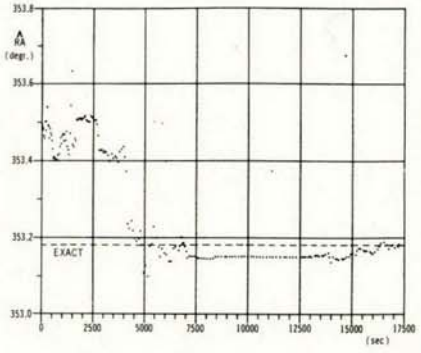

Fig. 9 Estimated right ascension of spin axis direction (simulation free-drift 4)

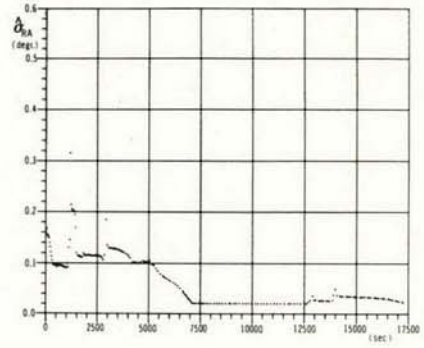

Fig. 10 Estimated standard deviation of spin axis right ascension (simulation free-drift 4)

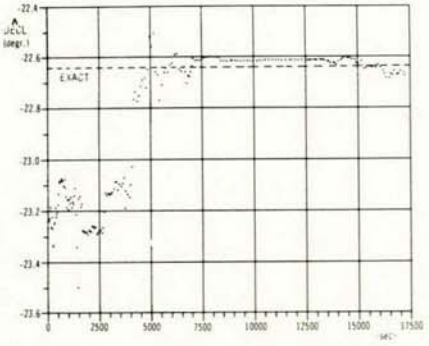

Fig. 11 Estimated declination of spin axis direction (simulation free-drift 4)

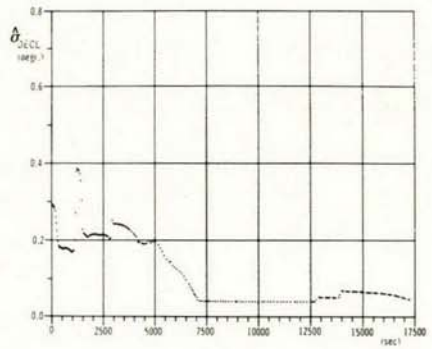

Fig. 12 Estimated standard deviation of spin axis declination (simulation free-drift 4)

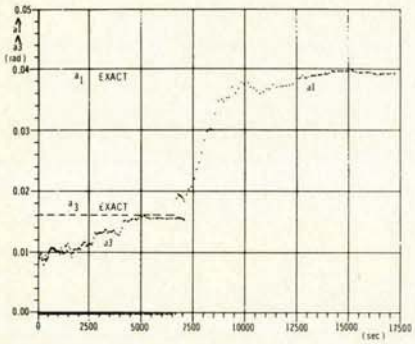

Fig. 13 Estimated delay parameters a_1 and a_3 of first and third earth chord delay (simulation free-drift 4)

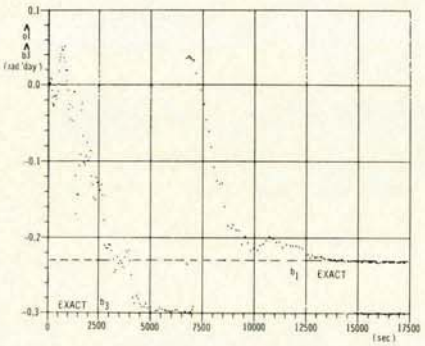

Fig. 14 Estimated delay parameters b_1 and b_3 of first and third earth chord delay (simulation free-drift 4)

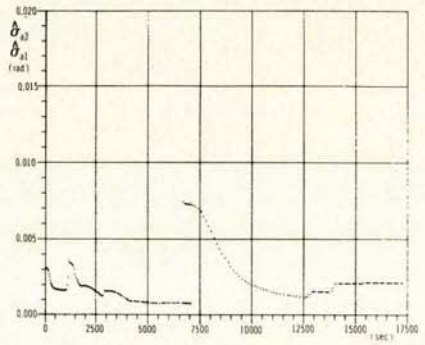

Fig. 15 Estimated standard deviations of earth chord delay parameters a_1 and a_3 (simulation free-drift 4)

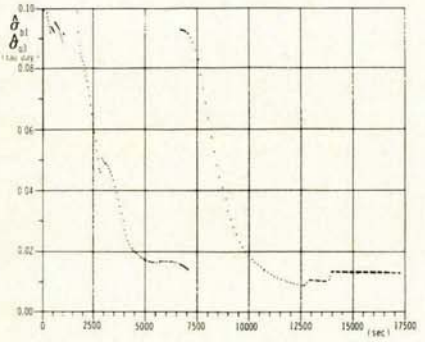

Fig. 16 Estimated standard deviations of earth chord delay parameters b_1 and b_3 (simulation free-drift 4)

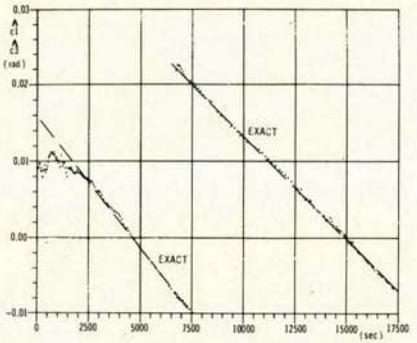

Fig. 17 Exact and estimated earth chord delays of first and third earth sensor (simulation free-drift 4)

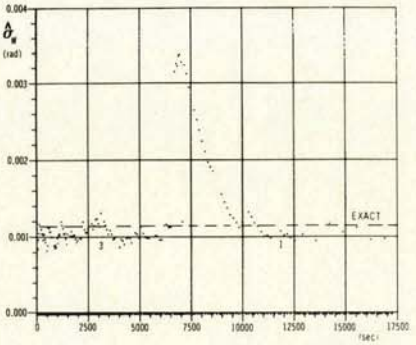

Fig. 18 Estimated measurement noise standard deviation of earth chord measurements of first and third earth sensor (simulation free-drift 4)

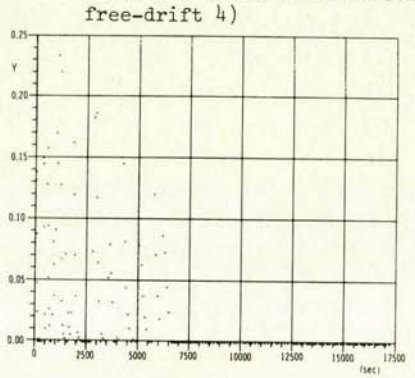

Fig. 19 Divergence monitoring parameter of earth chord measurements of third earth sensor (simulation free-drift 4)

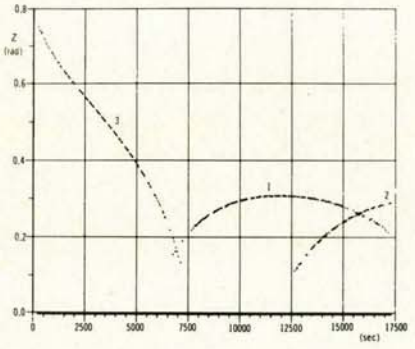

Fig. 20 Real earth chord measurements (real free-drift 4)

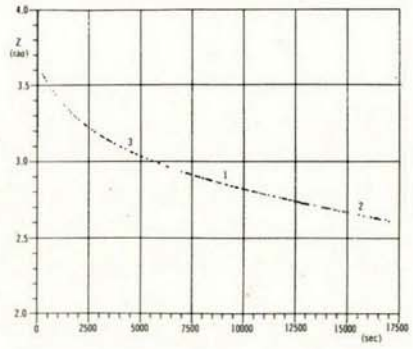

Fig. 21 Real midscan rotation angle measurements (real free-drift 4)

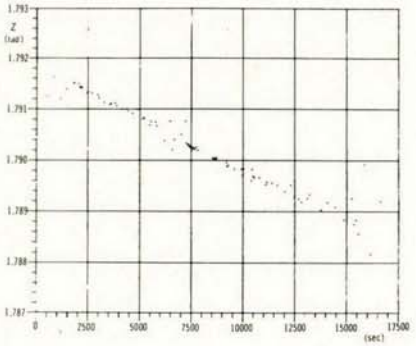

Fig. 22 Real sun measurements (real free-drift 4)

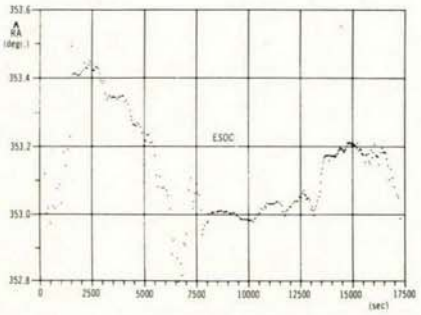

Fig. 23 Estimated right ascension of spin axis direction (real free-drift 4, case 1)

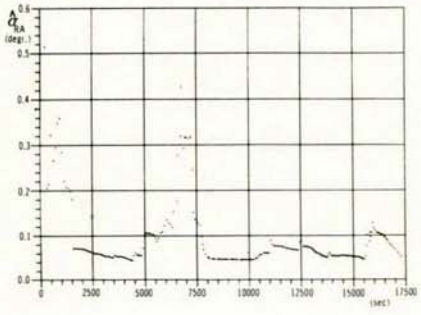

Fig. 24 Computed standard deviation of estimated spin axis right ascension (real free-drift 4, case 1)

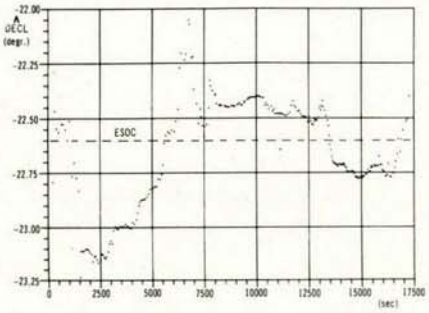

Fig. 25 Estimated declination of spin axis direction (real free-drift 4, case 1)

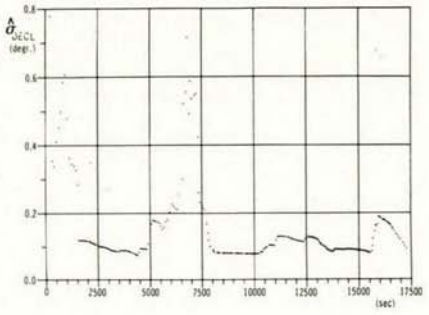

Fig. 26 Computed standard deviation of estimated spin axis declination (real free-drift 4, case 1)

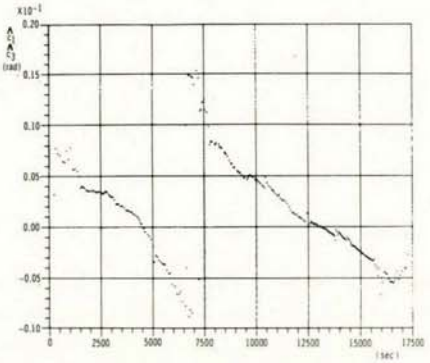

Fig. 27 Estimated earth chord delays of first and third earth sensor (real free-drift 4, case 1)

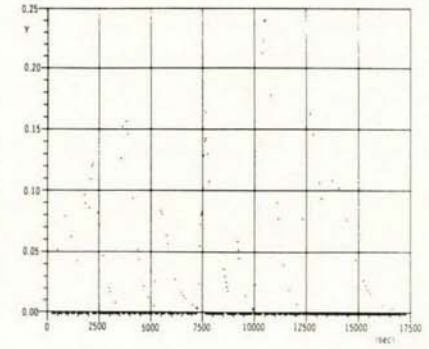

Fig. 28 Divergence monitoring parameter of sun sensor (real free-drift 4, case 1)

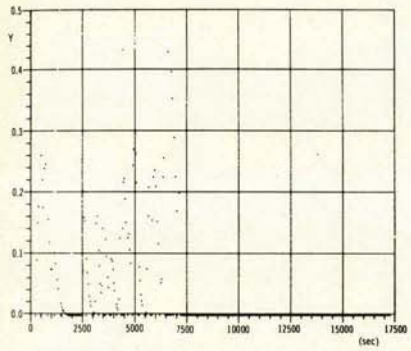

Fig. 29 Divergence monitoring parameter of earth chord measurements of third earth sensor (real free-drift 4, case 1)

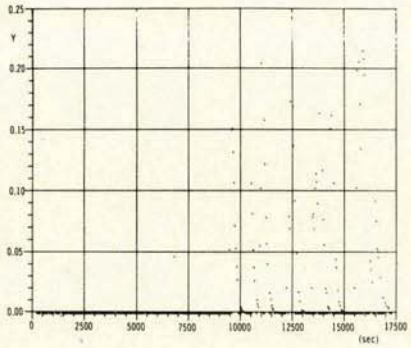

Fig. 30 Divergence monitoring parameter of earth chord measurements of first earth sensor (real free-drift 4, case 1)

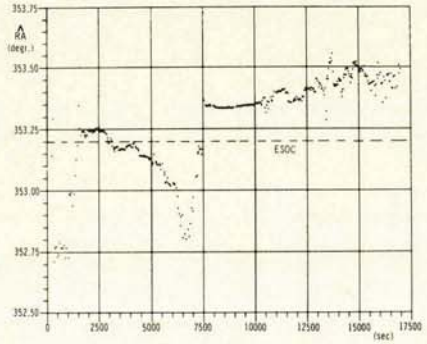

Fig. 31 Estimated right ascension of spin axis direction (real free-drift 4, case 2)

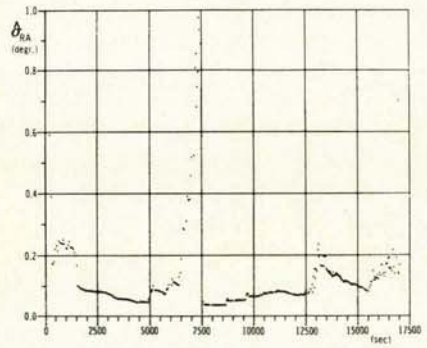

Fig. 32 Computed standard deviation of estimated spin axis right ascension (real free-drift 4, case 2)

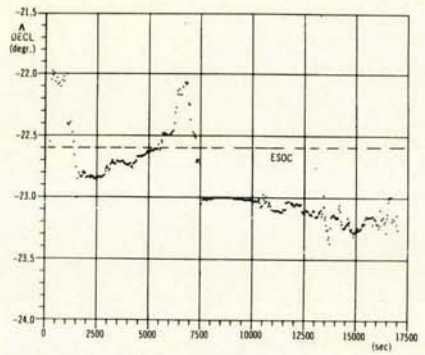

Fig. 33 Estimated declination of spin axis direction (real free-drift 4, case 2)

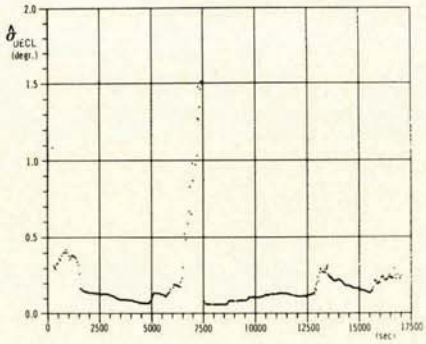

Fig. 34 Computed standard deviation of estimated spin axis declination (real free-drift 4, case 2)

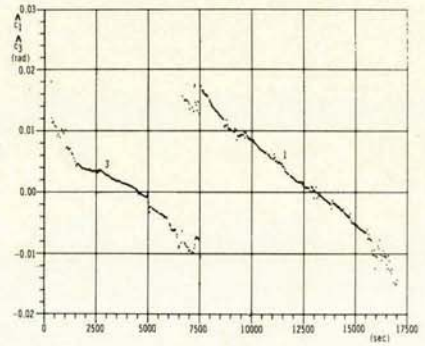

Fig. 35 Estimated earth chord delays of first and third earth sensor (real free-drift 4, case 2)

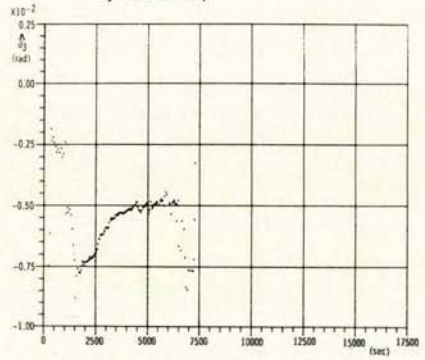

Fig. 36 Estimated delay of midscan rotation angle measurements of third earth sensor (real free-drift 4, case 2)

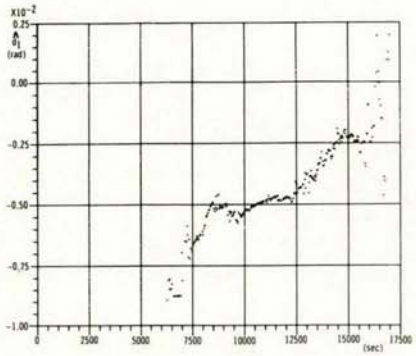

Fig. 37 Estimated delay of midscan rotation angle measurements of first earth sensor (real free-drift 4, case 2)

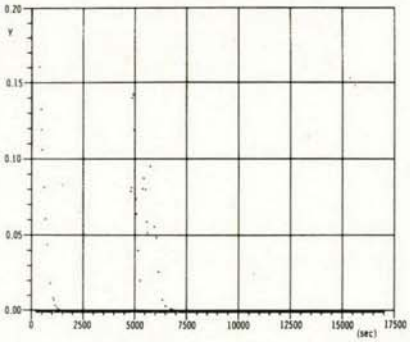

Fig. 38 Divergence monitoring parameter of midscan rotation angle measurements of third earth sensor (real free-drift 4, case 2)

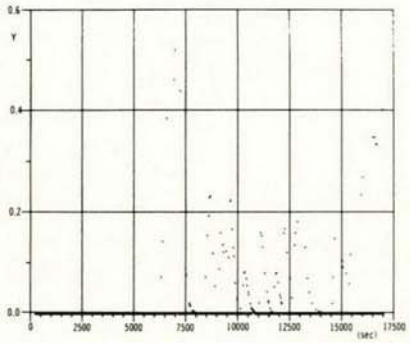

Fig. 39 Divergence monitoring parameter of midscan rotation angle measurements of first earth sensor (real free-drift 4, case 2)

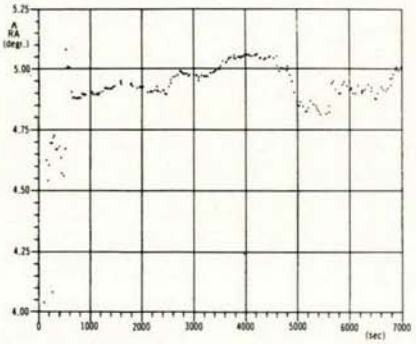

Fig. 40 Estimated right ascension of spin axis direction (real free-drift 2, case 1)

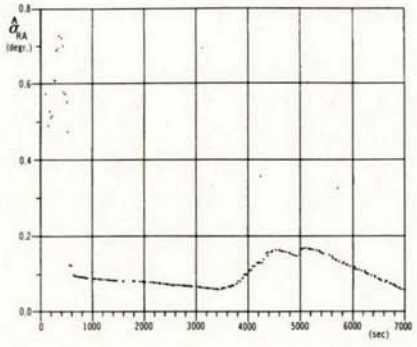

Fig. 41 Computed standard deviation of estimated spin axis right ascension (real free-drift 2, case 1)

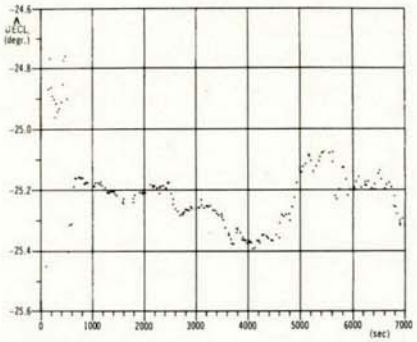

Fig. 42 Estimated declination of spin axis direction (real free-drift 2, case 1)

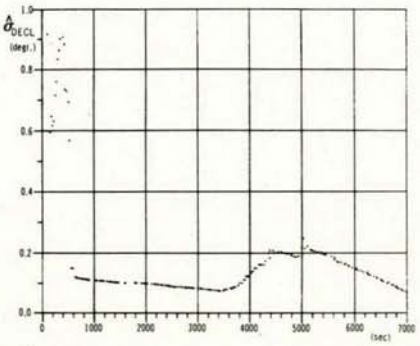

Fig. 43 Computed standard deviation of estimated spin axis declination (real free-drift 2, case 1)

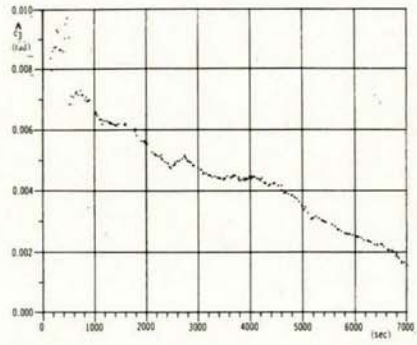

Fig. 44 Estimated earth chord delay of third earth sensor (real free-drift 2, case 1)

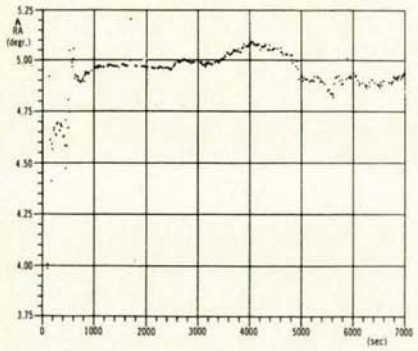

Fig. 45 Estimated right ascension of spin axis direction (real free-drift 2, case 2)

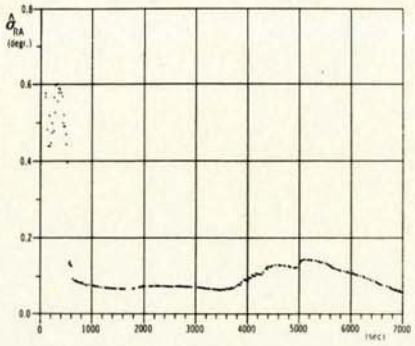

Fig. 46 Computed standard deviation of estimated spin axis right ascension (real free-drift 2, case 2)

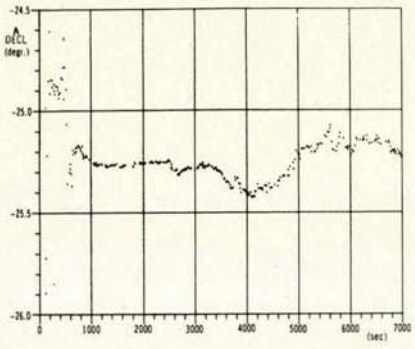

Fig. 47 Estimated declination of spin axis direction (real free-drift 2, case 2)

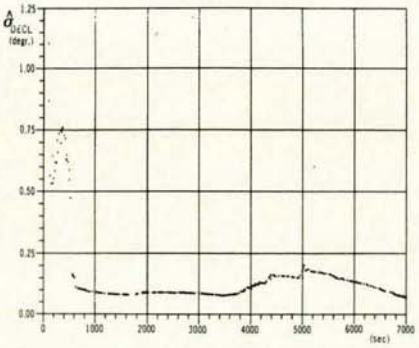

Fig. 48 Computed standard deviation of estimated spin axis declination (real free-drift 2, case 2)

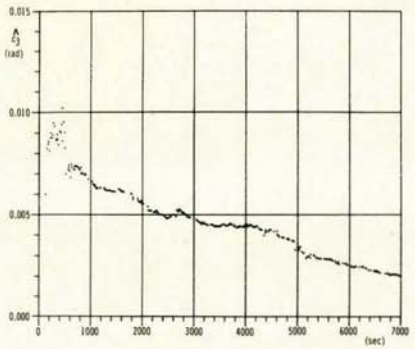

Fig. 49 Estimated earth chord delay of third earth sensor (real free-drift 2, case 2)

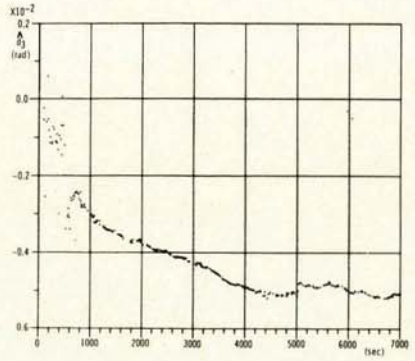

Fig. 50 Estimated delay of midscan rotation angle measurements of third earth sensor (real free-drift 2, case 2)